ROYAL SOCIETY
OF CHEMISTRY

COMMUNICATION

Check for updates

A medicine-inspired hydroxyl-rich equimolar ZnSO₄/D-mannitol electrolyte enables horizontally stacked Zn deposition for long-cycling aqueous batteries†

Jin Xiao,‡ Chenbo Yuan,‡ Cong Liu, Ximei Sun, Bing Cheng, Zitong Huang, Xiaowen Zhan [ID] * and Lingyun Zhu*

Dendrite growth and adverse side reactions at the Zn anode often compromise the cycling stability and lifespan of aqueous Zn-metal batteries (AZMBs). Inspired by the high osmotic dehydration effect in medicine, this study introduces an equimolar ZnSO₄/D-mannitol (MNT) electrolyte to stabilize the Zn anodes. Comprehensive spectrochemical characterization and theoretical calculations, coupled with rigorous electrochemical and electroanalytical tests, show that the hydroxyl-rich MNT strongly interacts with water, reducing hydrogen bonds and reshaping solvation structures of hydrated Zn^{2+}, thereby effectively suppressing corrosion and side reactions. Furthermore, the preferential adsorption of MNT at the Zn anode surface regulates the interfacial reaction environment, enabling dendrite-free, orderly-stacked and corrosion-less Zn deposition. This is confirmed by backscattered-electron scanning electron microscopy observations on cycled electrodes prepared using a cross-section polisher. As a result, the use of a D-mannitol-enriched ZnSO₄ electrolyte extends the cycle life of Zn||Zn symmetric cells to over 2980 hours and significantly enhances the long-term cycling performance of Zn||PANI (polypyrrole–polyaniline) full cells at a low N/P ratio of 22.48.

1. Introduction

Aqueous zinc-metal batteries (AZMBs) have emerged as strong contenders for the next generation of large-scale energy storage due to the low redox potential of zinc (Zn) anodes (−0.762 V *vs.* standard hydrogen electrode, SHE), their high theoretical capacity (820 mA h g^{-1}, 5851 mA h cm^{-3}) and their inherent safety in water-based environments.[1] However,

challenges arise due to the strong affinity of Zn^{2+} ions for forming $[Zn(H_2O)_6]^{2+}$ solvation structures with water molecules in aqueous electrolytes, leading to uneven Zn deposition and dendrite growth.[2–4] Moreover, the thermodynamically unstable Zn in aqueous solutions is prone to corrosion and side reactions, such as hydrogen evolution reactions (HERs), which cause battery volume expansion and potential failure.[5] These issues significantly compromise the cycling stability and lifespan of AZMBs, posing obstacles to their practical use.

Numerous strategies have been developed to address these challenges faced by AZMBs, including the construction of artificial interface layers,[6–9] designing anode architectures,[10,11] and electrolyte modifications.[12–14] While creating artificial interface layers and designing anode architectures are often complex and time-intensive processes, electrolyte engineering such as adding electrolyte additives presents a simpler, direct, and cost-effective alternative.[15,16] Currently, electrolyte modifications cover five main approaches: (1) forming hydrogen bonds with water to reduce its activity and thus mitigate corrosion and HERs;[17,18] (2) altering the solvation shell of Zn^{2+} ions to regulate their solvation structures;[19,20] (3) adsorbing onto the Zn anode surface to promote uniform Zn^{2+}-deposition;[21,22] (4) creating *in situ* solid electrolyte interphase (SEI) layers on the Zn anode to protect against electrolyte attack;[23–26] (5) accumulating at the tips of the Zn anode to establish an electrostatic shield.[27,28] Although these strategies have notably improved the stability of Zn anodes, their effectiveness is generally focused on one aspect and falls short of the comprehensive requirements for high-performance AZMBs. Therefore, there is still a critical need to develop an environmentally sustainable, cost-effective, and versatile electrolyte modification strategy to advance AZMB technology.

In medicine, D-mannitol (MNT), a monosaccharide macromolecule, is widely used as a dehydrating agent due to

School of Materials Science and Engineering, Key Laboratory of Structure and Functional Regulation of Hybrid Materials of Ministry of Education, Anhui University, 230601 Hefei, Anhui, PR China. E-mail: xiaowen.zhan@ahu.edu.cn, 22149@ahu.edu.cn

‡ J. Xiao and C. Yuan contributed equally to this work.
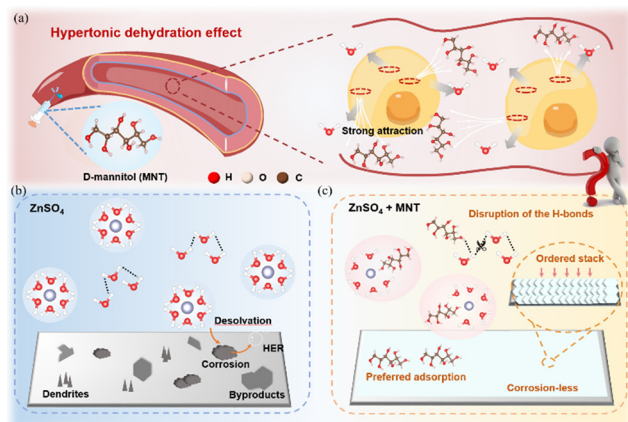
Fig. 1 (a) Schematic diagram of the mechanism by which increased osmotic pressure in MNT causes tissue dehydration. Schematic illustration of Zn^{2+} solvation structures and interfacial chemistry at Zn anodes in (b) $ZnSO_4$ and (c) $ZnSO_4$ + MNT electrolytes.

its significant osmotic effects, which are also common in various plants.[29] Its ability to promote water reflow from brain tissue into blood vessels results in brain tissue dehydration (Fig. 1a). Before this, Zhang *et al.* introduced trace amounts (0.02 M) of MNT into a 2 M $ZnSO_4$ solution, demonstrating the ability of MNT to reconstruct the solvation structure of Zn^{2+} and inhibit dendritic growth on the Zn anode surface.[30] However, the trace amount of MNT failed to disrupt the hydrogen bond network between active water molecules, and its role in modulating the anode/electrolyte interface was limited. Inspired by the effect of high concentrations of MNT molecules in increasing the attraction to water, we have incorporated MNT at an equimolar concentration into the conventional 1 M $ZnSO_4$ aqueous electrolyte to explore its modification mechanism (Fig. 1b and c). Through spectral analysis, molecular dynamics (MD) simulations and density functional theory (DFT) calculations, we have found that MNT increases the electrolyte's affinity for water, forming hydrogen bonds with water molecules and disrupting the original electrolyte's hydrogen bond network. Furthermore, MNT can integrate into the solvation structure of Zn^{2+}, replace an active water molecule, and reshape the solvation structure, effectively reducing corrosion and side reactions. Additionally, MNT's preferential adsorption on the Zn anode surface facilities uniform Zn^{2+} deposition along the (002) crystal plane. Leveraging an advanced backscattered-electron scanning electron microscope (BSE-SEM) coupled with a cross-section polisher (CP), we have observed a unique orderly stacked deposition structure free of dendrites and heavy corrosion enabled by MNT. As a result, both symmetric cells and full cells with MNT exhibit significantly improved cycling performances. The present work successfully applies the concept of MNT locking water for tissue dehydration to improving the performance of AZMBs, offering a promising avenue for future research.

2. Results and discussion

2.1 Strong MNT/H_2O interactions and reshaped solvation structures of Zn^{2+}

MNT is a polyol, each molecule of which contains six hydroxyl groups. We prepared 1 M $ZnSO_4$ aqueous electrolytes with varying concentrations of MNT (denoted as "*x*-MNT", *x* = 0.01, 0.1, 0.5, 1, 2). As depicted in Fig. S1a,† the pure 1 M $ZnSO_4$ solution is clear and transparent. However, as the concentration of added MNT increases to 2 M, the solution becomes turbid, indicating the oversaturation of MNT at this concentration. Additionally, we measured the pH and ion conductivity of the above solutions (Fig. S1b†). With the increase of MNT concentration, both the pH value and ion conductivity of the solutions slightly decrease, indicating that MNT primarily exists in the solutions in molecular form.

Hydroxyl groups in MNT can form hydrogen bonds with active water molecules in aqueous solution, thereby suppressing water activity and enhancing thermodynamic stability.[31] To explore the influence of the abundant hydroxyl groups in MNT molecules on the hydrogen bond network, we conducted nuclear magnetic resonance (NMR) tests on electrolyte solutions with different MNT concentrations. As shown in Fig. 2a, as the MNT concentration increases, the ^2H peak shifts from 4.681 ppm to 4.683 ppm, indicating a reduction in the number of free water molecules.[32] This suggests the formation of hydrogen bonds between MNT and H_2O, disrupting the original hydrogen bond network among water molecules. Further definitive evidence is provided by FT-IR and Raman spectroscopy. The FT-IR spectra (Fig. 2b) show a blue shift in the stretching vibration peak of O–H with increasing MNT concentration, confirming a decrease in
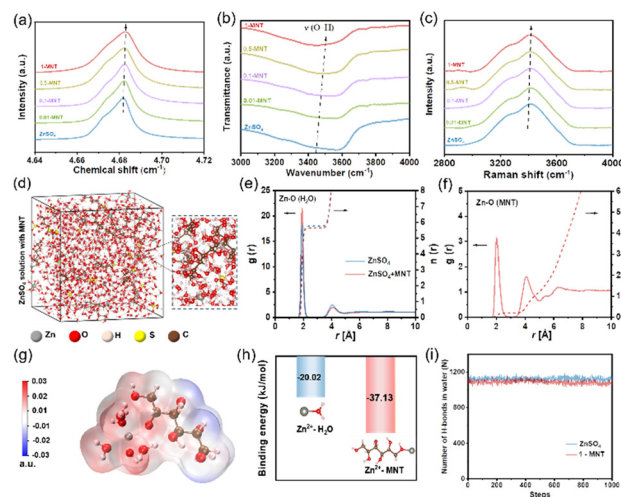
Fig. 2 (a) ^2H NMR spectra of D_2O, (b) FT-IR spectra and (c) Raman spectra (*v*-OH band) of 1 M $ZnSO_4$ electrolytes with various MNT concentrations. (d) Snapshot from MD simulation of the 1-MNT electrolyte and the local enlargement. RDFs of (e) Zn–O (H_2O) and (f) Zn–O (MNT) in different systems. (g) ESP distribution of the $[Zn(H_2O)_5MNT]^{2+}$ solvation structure. (h) Binding energy of Zn^{2+}–H_2O and Zn^{2+}-MNT. (i) Number counts for hydrogen-bonds inside $ZnSO_4$ and 1-MNT electrolytes.

water activity.[12] Peaks corresponding to hydrogen bond vibrations in the Raman spectra also shifts to higher wavenumbers (Fig. 2c), further corroborating the strong interaction between MNT and H_2O.

To explore the modulation effect of MNT on the solvation structure of Zn^{2+}, we conducted molecular dynamics (MD) simulations and constructed models for pure $ZnSO_4$ and 1-MNT solution systems. In the $ZnSO_4$ system, the typical solvation structure for Zn^{2+} is represented as $[Zn(H_2O)_6]^{2+}$ (Fig. S2a†). Upon the addition of MNT, one MNT molecule integrates into the solvation shell, displacing a water molecule (Fig. 2d). This change was further substantiated by the analysis of radial distribution functions (RDFs) and coordination number (CN) distribution functions. A Zn^{2+}–O (H_2O) peak appears at the first solvation shell with a radius of 2. With MNT present, the average CN of Zn^{2+} with H_2O decreases from 5.75 to 5.62 (Fig. 2e), and a new peak with a CN of 0.2 emerges for Zn^{2+}–O (MNT) (Fig. 2f), confirming the formation of $[Zn(H_2O)_5MNT]^{2+}$. The electrostatic potential (ESP) of the solvation shell, as derived from MD simulations, was also calculated (Fig. 2g and S2b†). The substitution of one H_2O molecule by MNT in the original $[Zn(H_2O)_6]^{2+}$ structure results in the ESP of $[Zn(H_2O)_5MNT]^{2+}$ being divided into distinct positive and negative regions, which enhances the transmission speed of solvated molecules under electrostatic interactions from the external environment. Further investigations using density functional theory (DFT) examined the interactions between Zn^{2+}, H_2O and MNT molecules. The binding energy between Zn^{2+} and MNT was found to be significantly higher than that between Zn^{2+} and H_2O (-37.13 kJ mol^{-1} vs. -20.02 kJ mol^{-1}, Fig. 2h), indicating a more energetically favorable interaction between Zn^{2+} and MNT molecules. Additionally, the number of hydrogen bonds within each system was quantified (Fig. 2i). The addition of MNT resulted in a decrease in the number of hydrogen bonds among H_2O molecules, which aligns with the spectral analysis previously discussed.

2.2 Anode/electrolyte interface regulation induced by MNT adsorption

In addition to altering the solvation structure, MNT plays a crucial role in regulating the anode/electrolyte interface. Tafel curves were used to evaluate the corrosion resistance of Zn electrodes in the two electrolytes, and the corrosion current density was obtained by extrapolating polarization curves in the strong polarization region (Fig. 3a). The Zn electrode in the 1-MNT electrolyte exhibits a lower corrosion current density (1.826 mA cm^{-2}) than that in pure $ZnSO_4$ (3.121 mA cm^{-2}). To further explore the anti-corrosion ability of MNT, polished Zn foils were immersed in $ZnSO_4$ and x-MNT (x = 0.01, 0.1, 0.5, 1 M) solutions for 5 days. Scanning electron microscopy (SEM) images reveal the presence of corrosion products on the surfaces of Zn foils immersed in the abovementioned solutions (Fig. 3b and S3†). Intriguingly, with increasing MNT concentration, these corrosion products
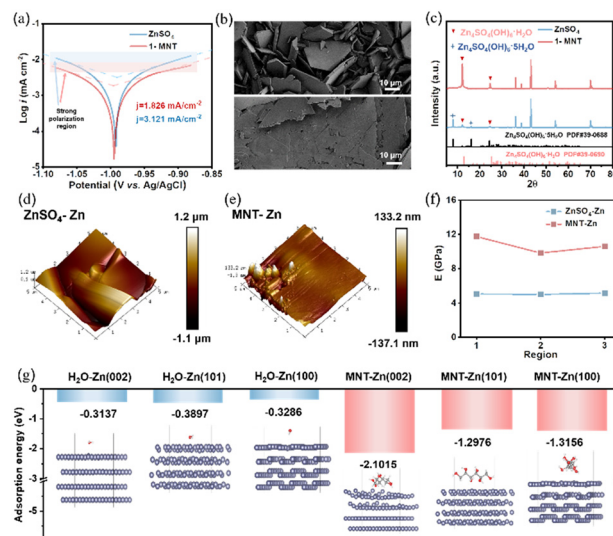
Fig. 3 (a) Comparison of Tafel plots of different electrolyte systems. (b) SEM images and (c) XRD spectra of Zn electrodes after soaking in $ZnSO_4$ and 1-MNT electrolytes for 5 days. AFM maps of the Zn surfaces after soaking in (d) $ZnSO_4$ and (e) 1-MNT electrolytes for 5 days. (f) Young's modulus of three regions selected on Zn plates after soaking in $ZnSO_4$ and 1-MNT electrolytes for 5 days. (g) Adsorption energy comparison of H_2O and MNT molecules on various Zn crystal planes.

shift from standard hexagonal plate-like structures to irregular, fragmented shapes. At a concentration of 1 M MNT, the corrosion products on the Zn foil surfaces transform into relatively flat, leaf-like shapes (Fig. S4†). We employed X-ray Diffraction (XRD) to analyze the surface material composition of Zn plates immersed in $ZnSO_4$ (denoted as "ZnSO$_4$-Zn") and 1-MNT (denoted as "MNT-Zn") solutions for 5 days. The XRD results reveal that the corrosion products on ZnSO$_4$-Zn primarily consists of Zn_4-$SO_4(OH)_6 \cdot 5H_2O$, while those on MNT-Zn are highly crystalline $Zn_4SO_4(OH)_6 \cdot H_2O$ (Fig. 3c). This difference likely stems from the reduced amount of free water in the solution, due to the strong interaction between MNT and H_2O.

To further examine the physical properties of the corrosion products, we utilized atomic force microscopy (AFM) to analyze the surface structures of both Zn foils. The ZnSO$_4$-Zn surface is notably irregular and uneven, while the MNT-Zn surface appear relatively flat and smooth (Fig. 3d and e). We also measured the Young's modulus in three distinct regions of each sample (Fig. 3f and S5†). The findings indicate that the Young's modulus of MNT-Zn is more than twice that of ZnSO$_4$-Zn, suggesting that the corrosion products formed in the 1-MNT solution are dense and compact, potentially enhancing the corrosion resistance of the Zn anode. To assess whether the corrosion products in the 1-MNT electrolyte impact the transport of Zn^{2+}, we conducted electrochemical impedance spectroscopy (EIS) on symmetric cells left for different durations. Results illustrated in Fig. S6† indicate that the charge-transfer resistance of symmetric cells using the $ZnSO_4$ electrolyte increased significantly after 5 days. In contrast, symmetric cells with

the 1-MNT electrolyte display relatively stable charge-transfer resistance, suggesting that the corrosion products in the 1-MNT electrolyte enhance the stability of the Zn electrode. To further examine the protective effects of these corrosion products, Zn foils immersed in the $ZnSO_4$ and 1-MNT electrolytes for five days were assembled into symmetric cells with the $ZnSO_4$ electrolyte and tested (Fig. S7†). The finding demonstrates that the MNT-Zn||MNT-Zn symmetric cell maintained stable operation for over 2300 hours, confirming that the corrosion products in the MNT-modified electrolyte act as barriers for the Zn anode, mitigating adverse reactions between the electrolyte and the Zn anode and thus improving interfacial stability.

To verify the preferential adsorption of MNT on the Zn anode surface, the double-layer capacitance (EDLC) of the Zn anode was initially tested (Fig. S8†). The EDLC value significantly decreases from 0.21 to 0.14 mF cm^{-2} following the addition of MNT, indicating an increase in the thickness of the electric double layer (EDL) due to MNT adsorption.[33] DFT calculations were performed to analyze the adsorption energies of H_2O and MNT on three major crystal planes of Zn, further corroborating these observations. As depicted in Fig. 3g, the adsorption energies of MNT on all crystal planes significantly exceed those of H_2O, highlighting the strong preferential surface adsorption of MNT on the Zn surface. Notably, the adsorption energy of MNT on Zn (002) is the highest at −2.1015 eV. Drawing on previous research, we deduce that the crystal growth direction of Zn metal is closely associated with the orientation of its crystal faces.[34–36] This insight suggests that there are favorable conditions for plane deposition of Zn along the (002) direction. To provide macroscopic evidence of MNT's affinity to Zn, contact angle measurements were performed as displayed in Fig. S9.† The introduction of MNT reduces the contact angle from 90.1° to 60.2°. This significant decrease suggests that the 1-MNT electrolyte improves the wetting properties on the Zn foil, possibly due to MNT adsorption reducing the surface energy.[37] These findings demonstrate that MNT effectively modifies the electrode/electrolyte interface environment by preferentially adsorbing onto the Zn foil surface, thereby mitigating side reactions and promoting uniform Zn deposition during cycling.

2.3 Effect of MNT on the kinetics and morphology of Zn^{2+} deposition

Building on the previous adjustments related to solvation and corrosion inhibition effects, as well as through a comprehensive comparison of the electrochemical performance of symmetrical cells, we have determined that the optimal concentration of MNT is 1 M, hereafter denoted as "$ZnSO_4$ + MNT". We tracked changes at the Zn electrode interface during the constant-current plating in both $ZnSO_4$ and $ZnSO_4$ + MNT electrolytes using *in situ* optical microscopy (Fig. 4a). In the $ZnSO_4$ electrolyte, noticeable protrusions appeared on the surface after 30 minutes of electroplating, which worsened over time.
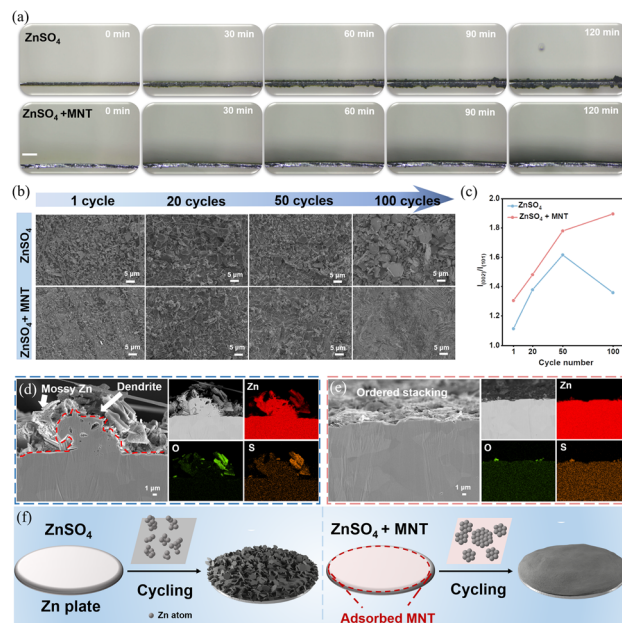
Fig. 4 (a) *In situ* optical observations of the Zn deposition process at a current density of 1 mA cm^{-2} in the $ZnSO_4$ and $ZnSO_4$ + MNT electrolytes. Scale bar: 200 μm (b) SEM images of Zn electrodes after different cycles at 1 mA cm^{-2} and 1 mA h cm^{-2} in $ZnSO_4$ and $ZnSO_4$ + MNT electrolytes. (c) Line chart for the ratio of $I_{(002)}/I_{(101)}$ planes. Cross-sectional BSE-SEM images and corresponding EDX maps of the cycled Zn electrode after 100 cycles in (d) $ZnSO_4$ and (e) $ZnSO_4$ + MNT electrolytes at 1 mA cm^{-2} and 1 mA h cm^{-2}. (f) Schematic of the preferential growth of the (002) plane induced by MNT during cycling of AZMBs.

Additionally, it was observed that dendritic growth was most vigorous at the initial sites of these protrusions, confirming that Zn^{2+} ions are preferentially plated at the tips due to the uneven distribution of the electric field. After 120 minutes, visible bubbles indicated the occurrence of the HER during plating. Conversely, uniform and dense Zn deposition was observed on the Zn electrode in the $ZnSO_4$ + MNT electrolyte within two hours of electroplating. This confirms that the adsorption of MNT on the Zn electrode surface helps distribute the electric field, effectively regulating the electroplating behavior of Zn^{2+} and suppressing dendritic growth and the HER. Linear sweep voltammetry (LSV) was used to assess HER kinetics before and after the addition of MNT (Fig. S10†). Notably, the HER onset potential shifted from −1.164 V to −1.226 V (*vs.* Ag/AgCl) at 20 mA cm^{-2} after introducing MNT, indicating a significant inhibition of HER kinetics.

The influence of MNT on the nucleation and growth of Zn was examined using chronoamperometry (CA) as depicted in Fig. S11.† The current response in symmetrical cells with the $ZnSO_4$ electrolyte was noted to decline rapidly, indicating uncontrolled 2D diffusion of Zn^{2+} on the Zn surface. Conversely, with the $ZnSO_4$ + MNT electrolyte, the current stabilized after 20 seconds, suggesting a swift transition from 2D disorderly diffusion to 3D stable diffusion.[38] To quantitatively assess the kinetics of Zn^{2+} deposition, we calculated the dissolution activation energy (E_a) for Zn^{2+} as

shown in Fig. S12.†[39] Additionally, impedance measurements of symmetrical cells at different temperatures showed an increase in charge transfer resistance when MNT was added to the electrolyte. This suggests that MNT decelerates the charge transfer kinetics on the Zn anode surface. Furthermore, using the Arrhenius equation, we determined the dissolution activation energy (E_a) of Zn^{2+} on the anode surface. The results indicated that the energy barrier required for Zn^{2+} transfer in the $ZnSO_4$ + MNT electrolyte is higher (29.90 vs. 24.13 kJ mol^{-1}), thereby corroborating the adsorption of MNT on the Zn anode surface and effectively inhibiting the 2D disorderly diffusion of Zn^{2+} across the electrode surface.

To further elucidate MNT's role in regulating Zn^{2+} deposition, we examined the micro-morphological changes on the surface of Zn anodes in symmetric cells after various numbers of cycles using SEM. As depicted in Fig. 4b, after just one cycle in the $ZnSO_4$ electrolyte, the Zn anode surface featured numerous irregularly arranged dendritic flakes. Moreover, with an increase in the number of cycles, the dendritic flakes' thickness continued to grow, accompanied by a significant presence of by-products scattered across the Zn anode surface. In contrast, the Zn anode cycled in the $ZnSO_4$ + MNT electrolyte maintained a smooth and dense surface. The elemental composition of the Zn anode surface after 100 cycles was analyzed using energy dispersive X-ray spectroscopy (EDX). Notably, a sulfur (S) mass fraction as high as 4.3% was detected on the surface of the Zn anode cycled in the $ZnSO_4$ electrolyte, indicating a substantial accumulation of $Zn_4SO_4(OH)_6 \cdot xH_2O$ by-products (Fig. S13†). Meanwhile, the S content measured on the Zn anode cycled in the $ZnSO_4$ + MNT electrolyte was significantly lower (Fig. S14†), which confirms MNT's effective role in suppressing by-product formation.

Interestingly, after cycling in the $ZnSO_4$ + MNT electrolyte, the Zn deposition on the Zn anode surface showed a distinct preferred orientation, forming a layered morphology, as confirmed by corresponding XRD spectra (Fig. S15†). The intensity ratio of $I_{(002)}/I_{(101)}$ on the Zn anode surface after cycling in the pure $ZnSO_4$ electrolyte displayed no consistent trend. However, with the addition of MNT, this ratio gradually increased with each cycle (from 1.3 to 1.9) (Fig. 4c). The (002) crystal plane is known to promote the deposition of Zn^{2+} parallel to the Zn anode surface. To visually examine the deposition morphology of Zn^{2+}, we conducted argon ion beam polishing on the cross-sections of the Zn anodes after 100 cycles and captured backscattered electron (BSE-SEM) images. The cross-sectional images from the Zn anode after 100 cycles in the $ZnSO_4$ electrolyte (Fig. 4d) revealed the growth of large dendrites along with moss-like dead Zn and hexagonal by-products on the dendrite surfaces. The significant accumulation of sulfur (S) detected in the EDX spectra of the Zn anode surface corroborated this observation. In contrast, after the introduction of MNT, the Zn deposited on the Zn anode surface after 100 cycles was orderly stacked, with only trace amounts of by-products

evident (Fig. 4e). Even at lower magnifications, dendrites were scarcely visible (Fig. S16†). Thus, the preferred (002) crystal plane in the $ZnSO_4$ + MNT electrolyte highlights MNT's role in regulating the Zn^{2+} deposition morphology, which is crucial in suppressing dendritic growth that arises from uneven electric field distribution during Zn^{2+} plating/ stripping processes.

2.4 Enhanced electrochemical performances of batteries with MNT

To validate the beneficial impact of MNT on enhancing the reversibility and stability of AZMBs, we assembled Zn||Zn symmetric cells with various concentrations of MNT to evaluate their long-term cycling performance (Fig. S17†). We can observe that the cycle life gradually increases with the rise in MNT concentration, which is consistent with the trend shown in Fig. 2a–c, indicating that the hydroxyl groups in MNT form hydrogen bonds with water, effectively suppressing side reactions and significantly enhancing the stability of the Zn anode. Notably, the symmetric cell with the 1 M MNT electrolyte demonstrated the longest cycle life, achieving over 2980 hours of cumulative plating/stripping
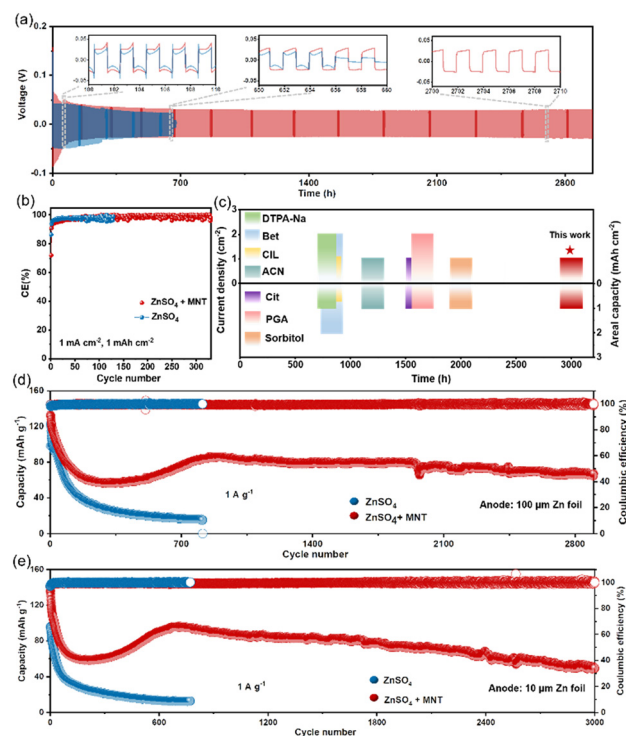
Fig. 5 (a) Long-term cycling stability of symmetrical cells at 1 mA h cm^{-2} and 1 mA cm^{-2}. The utilization of Zn: 1.81%. (b) Coulombic efficiencies of Zn plating/stripping in various electrolytes at 1 mA h cm^{-2} and 1 mA cm^{-2}. (c) Long-term symmetric-cell cyclability enabled by the $ZnSO_4$ + MNT electrolyte compared to those achieved via some representative electrolyte modifications under different cycling conditions. (d) Long-span cycling performances of Zn||PANI@CC full cells at 1 A g^{-1}. (e) Cycling performances of Zn||PANI@CC cells at 1 A g^{-1} at a low N/P ratio of 22.48.

© 2025 The Author(s). Published by the Royal Society of Chemistry

RSC Appl. Interfaces, 2025, **2**, 61–68 | **65**

time, which is five times longer than that of the pure $ZnSO_4$ electrolyte (Fig. 5a). The voltage curve of the symmetric cell using the $ZnSO_4$ electrolyte exhibited drastic fluctuations after 640 hours, which we suspect were due to dendrite formation and severe corrosion of the Zn anode, leading to short circuits. Examination of the cross-section of the Zn anode from the Zn||Zn symmetric cell with the $ZnSO_4$ electrolyte post-short circuit revealed large clusters of dendrites and dead Zn that had grown on the surface, with dendrites tall enough to puncture the separator and cause battery short circuits (Fig. S18†). Additionally, the Zn plate experienced severe corrosion, resulting in significant holes and structural collapse, supporting our initial conjecture.

It is noteworthy that the introduction of MNT slightly increased the initial overpotential from 56.7 mV to 64 mV, primarily due to the strong adsorption of MNT on the Zn anode surface (Fig. S19†). A higher nucleation overpotential provides a greater driving force for nucleation, which results in a reduced Zn nucleation radius and increased nucleation density, facilitating the formation of dense and flat deposition layers.[40] Even when the current density was increased to 5 mA cm^{-2}, the symmetric cell with the $ZnSO_4$ + MNT electrolyte maintained good cycling stability up to 430 hours (Fig. S20†). Fig. S21† illustrates the rate performance of the Zn||Zn symmetric cell with a fixed capacity of 1 mA h cm^{-2} at current densities ranging from 0.2 to 10 mA cm^{-2}. At lower current densities between 0.2 and 1 mA cm^{-2}, the overpotentials of both cells remained similar. However, as the current density exceeded 2 mA cm^{-2}, the overpotential of the symmetric cell with the $ZnSO_4$ electrolyte increased significantly.

Zn||Ti asymmetric cells were assembled to evaluate the coulombic efficiency (CE) of the Zn anode during cycling (Fig. 5b). The Zn||Ti cell with the $ZnSO_4$ + MNT electrolyte demonstrated an impressive average CE of 97.9% over 300 cycles at 1 mA cm^{-2} and 1 mA h cm^{-2}, indicating excellent reversibility of Zn plating/stripping processes. In contrast, the CE of the cell with the $ZnSO_4$ electrolyte plummeted to zero after just 100 cycles due to side reactions and dendritic growth. The detailed capacity–voltage curves are shown in Fig. S22.† The cell with the $ZnSO_4$ + MNT electrolyte exhibits higher reversibility and lower voltage polarization. To highlight the effectiveness of the MNT addition, we compared the cycling life of symmetric cells using MNT with other published electrolyte modifications for AZMBs under identical conditions of 1 mA cm^{-2} and 1 mA h cm^{-2} (Fig. 5c).[13,34,41–45] The results show that our $ZnSO_4$ + MNT electrolyte significantly outperforms these other modified electrolytes.

To further validate the practical effectiveness of the $ZnSO_4$ + MNT electrolyte, we employed PANI@CC (polypyrrole–polyaniline on carbon cloth) as the cathode material to assemble full cells for testing. SEM images and corresponding EDX mapping showed that PANI was uniformly dispersed on the fibers of the carbon cloth (Fig. S23†). In the cyclic voltammetry (CV) curves, the positions of the oxidation and reduction peaks overlapped, indicating a consistent charge storage mechanism of the PANI@CC cathode in both electrolyte systems (Fig. S24†). Long-term cycle performance tests of the full cells were conducted at a current load of 1 A g^{-1} (Fig. 5d), showcasing the robustness and reliability of the MNT-modified electrolyte in practical applications. The Zn||PANI@CC full cell with the $ZnSO_4$ electrolyte experienced continuous capacity decay from the onset of cycling and abruptly failed after the 814th cycle. Meanwhile, the full cell using the $ZnSO_4$ + MNT electrolyte achieved stable cycling for over 2900 cycles, with a capacity retention rate of 74.42% between cycles 830 and 2900. The voltage–capacity curves of the Zn||PANI@CC full cells with different electrolytes, as shown in Fig. S25,† indicate that the full cell with the $ZnSO_4$ + MNT electrolyte maintained closer charge–discharge curve intervals across various cycle numbers, suggesting that a higher capacity retention rate was achieved. The rate performance at different current densities ranging from 0.05 to 1 A g^{-1} further demonstrates the enhanced stability of the battery with the MNT-containing electrolyte (Fig. S26†). Additionally, while previously reported high-performance AZMBs often used excess Zn (over 100 μm) to achieve long cycle life, we conducted a more realistic evaluation using thinner Zn foils (10 μm). Testing at a low N/P ratio of 22.48, the Zn||PANI@CC full cell with the $ZnSO_4$ + MNT electrolyte still maintained stable cycling for over 3000 cycles at 1 A g^{-1}, whereas the cell with the $ZnSO_4$ electrolyte failed after just 772 cycles (Fig. 5e). These results underscore that the introduction of MNT significantly enhances the stability of the Zn anode, thereby improving the electrochemical performance of the full cell.

3. Conclusion

In this work, we proposed a novel equimolar aqueous $ZnSO_4$/MNT electrolyte, inspired by the hypertonic dehydration effect observed in medicine, to address the critical issues of dendrite growth and side reactions troubling the Zn anodes in aqueous batteries. In the $ZnSO_4$ + MNT electrolyte, the hypertonic dehydration effect significantly decreases the active water content, effectively inhibiting the water-induced corrosion and side reactions. Moreover, MNT plays a vital role in promoting the preferred (002) deposition orientation of Zn^{2+}, resulting in a unique and orderly stacked morphology free of dendritic structures. Zn||Zn symmetric cells utilizing the $ZnSO_4$ + MNT electrolyte demonstrate an ultra-long cycling life exceeding 2980 hours at 1 mA cm^{-2} and 1 mA h cm^{-2}. Furthermore, Zn||PANI@CC full cells show markedly improved cycling performances in terms of capacity output, retention rate and cycle life at both high and low N/P ratios. This study offers a fresh perspective on developing environmentally friendly and cost-effective electrolyte modification strategies, merging biomedical and chemical sciences to support sustainable energy utilization and green environmental protection.

Data availability

All the data related to the current submission entitled "A medicine-inspired hydroxyl-rich equimolar $ZnSO_4$/D-mannitol electrolyte enables horizontally stacked Zn deposition for long-cycling aqueous batteries" are available upon reasonable request directly from the authors *via* email to the corresponding authors.

Author contributions

J. Xiao: conceptualization, investigation, methodology, formal analysis, writing – original draft. C. Yuan: software, methodology, formal analysis. C. Liu: software, investigation, formal analysis. X. Sun: methodology, software. B. Cheng: investigation. Z. Huang: methodology. X. Zhan: conceptualization, methodology, data curation, writing – review & editing, supervision. L. Zhu: conceptualization, methodology, supervision.

Conflicts of interest

There are no conflicts to declare.

Acknowledgements

References

1 J. F. Parker, C. N. Chervin, I. R. Pala, M. Machler, M. F. Burz, J. W. Long and D. R. Rolison, *Science*, 2017, **356**, 415–418.

2 L. Ding, L. Wang, J. Gao, T. Yan, H. Li, J. Mao, F. Song, S. Fedotov, L.-Y. Chang, N. Li, Y. Su, T. Liu and L. Zhang, *Adv. Funct. Mater.*, 2023, **33**, 2301648.

3 J. Xiao, C. Yuan, L. Xiang, X. Li, L. Zhu and X. Zhan, *Chem. – Eur. J.*, 2024, **30**, e202304149.

4 V. Yufit, F. Tariq, D. S. Eastwood, M. Biton, B. Wu, P. D. Lee and N. P. Brandon, *Joule*, 2019, **3**, 485–502.

5 M. Li, Z. Li, X. Wang, J. Meng, X. Liu, B. Wu, C. Han and L. Mai, *Energy Environ. Sci.*, 2021, **14**, 3796–3839.

6 A. Chen, C. Zhao, J. Gao, Z. Guo, X. Lu, J. Zhang, Z. Liu, M. Wang, N. Liu, L. Fan, Y. Zhang and N. Zhang, *Energy Environ. Sci.*, 2022, **16**, 275–284.

7 J. Duan, J. Dong, R. Cao, H. Yang, K. Fang, Y. Liu, Z. Shen, F. Li, R. Liu, H. Li and C. Chen, *Adv. Sci.*, 2023, **10**, 2303343.

8 M. Zhao, Y. Lv, S. Zhao, Y. Xiao, J. Niu, Q. Yang, J. Qiu, F. Wang and S. Chen, *Adv. Mater.*, 2022, **34**, 2206239.

9 C. Yuan, C. Liu, X. Li, Y. Zhi, X. Zhan and S. Gao, *ACS Appl. Energy Mater.*, 2023, **6**, 1897–1905.

10 C. Cao, K. Zhou, W. Du, C. C. Li, M. Ye, Y. Zhang, Y. Tang and X. Liu, *Adv. Energy Mater.*, 2023, **13**, 2301835.

11 J. Yang, X. Xu, Y. Gao, Y. Wang, Q. Cao, J. Pu, F. Bu, T. Meng and C. Guan, *Adv. Energy Mater.*, 2023, **13**, 2301997.

12 G. Duan, Y. Wang, B. Luo, L. Sun, S. Zheng, J. Huang and Z. Ye, *Energy Storage Mater.*, 2023, **61**, 102882.

13 H. Ren, S. Li, B. Wang, Y. Zhang, T. Wang, Q. Lv, X. Zhang, L. Wang, X. Han, F. Jin, C. Bao, P. Yan, N. Zhang, D. Wang, T. Cheng, H. Liu and S. Dou, *Adv. Mater.*, 2023, **35**, 2208237.

14 Z. Cheng, K. Wang, J. Fu, F. Mo, P. Lu, J. Gao, D. Ho, B. Li and H. Hu, *Adv. Energy Mater.*, 2024, **14**, 2304003.

15 Z. Li and A. W. Robertson, *Battery Energy*, 2023, **2**, 20220029.

16 Z. Ye, Z. Cao, M. O. Lam Chee, P. Dong, P. M. Ajayan, J. Shen and M. Ye, *Energy Storage Mater.*, 2020, **32**, 290–305.

17 J. Xie, Z. Liang and Y.-C. Lu, *Nat. Mater.*, 2020, **19**, 1006–1011.

18 J. Cui, X. Liu, Y. Xie, K. Wu, Y. Wang, Y. Liu, J. Zhang, J. Yi and Y. Xia, *Mater. Today Energy*, 2020, **18**, 100563.

19 W. Deng, Z. Xu and X. Wang, *Energy Storage Mater.*, 2022, **52**, 52–60.

20 J. Hao, L. Yuan, C. Ye, D. Chao, K. Davey, Z. Guo and S.-Z. Qiao, *Angew. Chem.*, 2021, **60**, 7366–7375.

21 Y. Jin, K. S. Han, Y. Shao, M. L. Sushko, J. Xiao, H. Pan and J. Liu, *Adv. Funct. Mater.*, 2020, **30**, 2003932.

22 C. Sun, C. Wu, X. Gu, C. Wang and Q. Wang, *Nano-Micro Lett.*, 2021, **13**, 89.

23 C. Huang, X. Zhao, S. Liu, Y. Hao, Q. Tang, A. Hu, Z. Liu and X. Chen, *Adv. Mater.*, 2021, **33**, 2100445.

24 W. Yuan, G. Ma, X. Nie, Y. Wang, S. Di, L. Wang, J. Wang, S. Shen and N. Zhang, *Chem. Eng. J.*, 2022, **431**, 134076.

25 H. Dai, T. Sun, J. Zhou, J. Wang, Z. Chen, G. Zhang and S. Sun, *Nat. Commun.*, 2024, **15**, 8577.

26 D. Li, L. Cao, T. Deng, S. Liu and C. Wang, *Angew. Chem., Int. Ed.*, 2021, **60**, 13035–13041.

27 Z. Hu, F. Zhang, Y. Zhao, H. Wang, Y. Huang, F. Wu, R. Chen and L. Li, *Adv. Mater.*, 2022, **34**, 2203104.

28 W. Xu, K. Zhao, W. Huo, Y. Wang, G. Yao, X. Gu, H. Cheng, L. Mai, C. Hu and X. Wang, *Nano Energy*, 2019, **62**, 275–281.

29 W. Su, N. Jia, H. Li, H. Hao and C. Li, *Chin. J. Chem. Eng.*, 2017, **25**, 358–362.

30 D. Zhang, J. Cao, Z. Dai, R. Chanajaree, C. Yang, X. Wu, X. Zhang and J. Qin, *J. Mater. Chem. A*, 2023, **11**, 23779–23786.

31 S. Bai, Z. Huang, G. Liang, R. Yang, D. Liu, W. Wen, X. Jin, C. Zhi and X. Wang, *Adv. Sci.*, 2024, **11**, 2304549.

32 Y. Liu, Y. An, L. Wu, J. Sun, F. Xiong, H. Tang, S. Chen, Y. Guo, L. Zhang, Q. An and L. Mai, *ACS Nano*, 2023, **17**, 552–560.

33 L. M. Da Silva, L. A. De Faria and J. F. C. Boodts, *Electrochim. Acta*, 2001, **47**, 395–403.

34 C. Huang, J. Mao, S. Li, W. Zhang, X. Wang, Z. Shen, S. Zhang, J. Guo, Y. Xu, Y. Lu and J. Lu, *Adv. Funct. Mater.*, 2021, **33**, 2315855.

35 Z. Cai, J. Wang, Z. Lu, R. Zhan, Y. Ou, L. Wang, M. Dahbi, J. Alami, J. Lu, K. Amine and Y. Sun, *Angew. Chem., Int. Ed.*, 2022, **61**, e202116560.

36 W. Feng, Z. Liang, W. Zhou, X. Li, W. Wang, Y. Chi, W. Liu, D. Gengzang, G. Zhang, Q. Chen, P. Wang, W. Chen and S. Zhang, *Dalton Trans.*, 2023, **52**, 7457–7463.

© 2025 The Author(s). Published by the Royal Society of Chemistry

RSC Appl. Interfaces, 2025, **2**, 61–68 | **67**

37 J. Hao, J. Long, B. Li, X. Li, S. Zhang, F. Yang, X. Zeng, Z. Yang, W. K. Pang and Z. Guo, *Adv. Funct. Mater.*, 2019, **29**, 1903605.

38 M. Zhou, S. Guo, J. Li, X. Luo, Z. Liu, T. Zhang, X. Cao, M. Long, B. Lu, A. Pan, G. Fang, J. Zhou and S. Liang, *Adv. Mater.*, 2021, **33**, 2100187.

39 Y. Yang, C. Liu, Z. Lv, H. Yang, Y. Zhang, M. Ye, L. Chen, J. Zhao and C. C. Li, *Adv. Mater.*, 2021, **33**, 2007388.

40 H. Wang, H. Li, Y. Tang, Z. Xu, K. Wang, Q. Li, B. He, Y. Liu, M. Ge, S. Chen, T. Hao, G. Xing and Y. Zhang, *Adv. Funct. Mater.*, 2022, **32**, 2207898.

41 Y. Xia, R. Tong, J. Zhang, M. Xu, G. Shao, H. Wang, Y. Dong and C.-A. Wang, *Nano-Micro Lett.*, 2024, **16**, 82.

42 Z. Zheng, D. Ren, Y. Li, F. Kang, X. Li, X. Peng and L. Dong, *Adv. Funct. Mater.*, 2024, **34**, 2312855.

43 J. Zheng, B. Zhang, X. Chen, W. Hao, J. Yao, J. Li, Y. Gan, X. Wang, X. Liu, Z. Wu, Y. Liu, L. Lv, L. Tao, P. Liang, X. Ji, H. Wang and H. Wan, *Nano-Micro Lett.*, 2024, **16**, 145.

44 J. Chen, N. Liu, W. Dong, Y. Xu, Y. Cao, S. Zhang, J. Hou, H. Bi, T. Lin and F.-Q. Huang, *Adv. Funct. Mater.*, 2024, 2313925.

45 P. Sun, L. Ma, W. Zhou, M. Qiu, Z. Wang, D. Chao and W. Mai, *Angew. Chem., Int. Ed.*, 2021, **60**, 18247–18255.